Spatiotemporal Visualization of THz Near-Fields in Metamaterial Arrays

**Hannes Merbold · Andreas Bitzer ·
Florian Enderli · Thomas Feurer**

Abstract We present an experimental approach to record the spatiotemporal electric field distribution of coherent broadband THz pulses propagating through planar metamaterial arrays. The electric field can be measured with sub-wavelength precision within a volume that is several wavelengths in size, thus, having the potential to map the near-field to far-field transition of the resonant structures constituting the metamaterial. To demonstrate the potential we present measurements of THz pulses propagating through a planar array of double split-ring resonators and their inverse analogues.

1 Introduction

Metamaterials have been a topic of considerable interest in recent years. They consist of man-made structures with sub-wavelength dimensions and exhibit intriguing electromagnetic behavior such as negative refractive indices [1], perfect lensing [2], or invisibility cloaking [3]. These unprecedented phenomena are based on resonant electric and magnetic responses of the constituting elements to an incoming electromagnetic field. One of the most prominent

---

H. Merbold (✉) · A. Bitzer · F. Enderli · T. Feurer
Institute of Applied Physics, University of Bern,
Sidlerstrasse 5, CH-3012 Bern, Switzerland
e-mail: hannes.merbold@iap.unibe.ch

examples is an array of metallic rings with a gap, so called split-ring resonators (SRRs) [4]. These SRRs exhibit several resonant responses where a combination of charge accumulations and current flows of increasing order are excited on the structure [5]. The terahertz (THz) frequency range is of particular interest for the investigation of metamaterials since THz time-domain spectroscopy (THz TDS) techniques [6] can resolve the amplitude, phase, and polarization of the electromagnetic fields. On the other hand the sub-wavelength criterion corresponds to structure sizes on the 100 μm scale which can be readily fabricated. Using THz TDS the response of SRRs to an incoming light field has already been analyzed both in the far- [7–10] and in the near-field [11, 12]. Here we report on a different experimental approach based on THz polaritonics [13] that allows us to record the spatiotemporal evolution of THz pulses transmitted through and reflected from SRR arrays with very high spatial and temporal resolution. Moreover, the experimental arrangement is such that the transmitted and the reflected fields can be monitored in a volume around the SRR arrays which is several tens of wavelengths large and thus ideal to investigate the near-field to far-field transition. Using this technique we investigate the transmission process through arrays of SRR arrays and their inverse analogues. We show that both structures exhibit a complementary resonant behavior as predicted by Babinet's principle and that for each structure the spectral composition of the transmitted and reflected waveforms are complementary. Numerical simulations based on finite element methods are used to complement the experimental results.

2 Experiment

An in-depth description of the THz polaritonic approach can be found in [13]. Here we give a short overview. Phonon-polaritons are strongly coupled admixtures of electromagnetic waves and polar lattice vibrations in ionic crystals [14]. By focusing optical femtosecond laser pulses into $LiNbO_3$ crystals one can directly generate THz phonon-polaritons through optical rectification [15, 16]. The generated THz waveforms are approximately single cycle pulses [17] with a broad spectral content extending from 100 GHz to about 1.5 THz. Due to the inherently different refractive indices of the crystal at visible and THz frequencies the THz radiation is generated in a Cherenkov cone geometry. For $LiNbO_3$ the Cherenkov angle θ_c between the propagation direction of the pump and a vector normal to the THz wavefront is 64° meaning that the THz wave propagates primarily in lateral directions away from the excitation region. Rather than focusing the optical excitation pulse into the crystal we follow an experimental approach that was recently put forward in order to obtain high power THz electric field strengths [18, 19]. In this approach the pump beam is diffracted of a reflection grating and imaged into the crystal using a cylindrical lens in order to obtain a tilted pump pulse front. The tilt angle is adjusted to match $\pm\theta_c$ so that either the leftward or rightward propagating THz

wave is coherently amplified, i.e. its energy increases as it propagates under θ_c through the crystal.

A time delayed probe pulse traveling collinearly with the pump pulse through the crystal is used for THz wave imaging [20]. The detection process is based on the electro-optic effect where the THz electric field induces a change in the refractive index at an optical probe wavelength. Using optical pulses for both the generation and detection process guarantees an automatic synchronism of the THz and probe pulse velocities [17]. The forward wave vector components are phase-matched so that the probe pulse integrates over the induced refractive index change along the entire path through the crystal. The probe pulse is typically expanded so that it illuminates the entire sample region and experiences a local phase shift at those positions where it spatially overlaps with the THz field. The phase modulation is converted into an amplitude modulation through the Talbot effect while the probe pulse is transmitted onto a CCD camera for real-space imaging [21]. Since the wavelength of the probe pulse is significantly shorter than the wavelength of the THz electric field the waveforms can be sampled with very high spatial resolution. By additionally varying the time delay between the pump and the probe pulse the complete spatiotemporal evolution of the THz wave propagation can be monitored.

The electric field of the THz waves can also be coupled out into free space or be transmitted into a second crystal that is placed in proximity to the first. It is therefore possible to sandwich arbitrary substances or structures between two crystals and visualize the transmitted and reflected waveforms. A similar arrangement has recently been used to investigate the prospects and limitations of slit waveguide based THz near-field microscopy [22].

The SRR samples were fabricated by photolithographic structuring of a 400 nm thick gold layer on a x-cut LiNbO$_3$ wafer with 1 mm thickness. The structures consist of arrays of concentric double SRRs with dimensions as indicated in Fig. 1a. Both arrays of SRRs (Fig. 1b) as well as complementary structures that effectively consist of split-ring shaped apertures (Fig. 1c) were fabricated. We follow the terminology of Chen and coworkers [23] where "original" refers to the positive structures and "complementary" to the inverse analogues. After structuring the wafer was sawed into stripes which for the
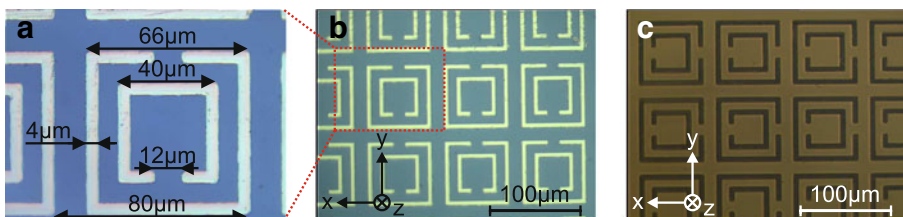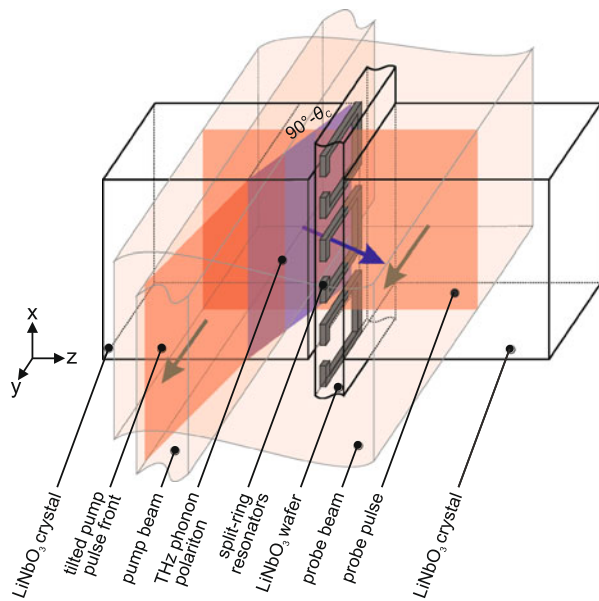

Fig. 1 Photographs of concentric double SRR arrays structured onto LiNbO$_3$. **a** Dimensions, **b** original SRRs, **c** complementary SRRs.

Fig. 2 Schematic illustration of the experimental configuration.

experiment were sandwiched between two LiNbO$_3$ crystals with dimensions of $10 \times 10 \times 3$ mm^3. Figure 2 shows a schematic illustration of the experimental configuration. THz pulses are generated through tilted pulse front excitation in the left crystal. A time-delayed probe pulse illuminating the entire sample region is used for THz electric field imaging. The pump and probe pulses are provided by an amplified Ti:sapphire laser system with a pulse width of 100 fs, a repetition rate of 500 Hz, and an average power of 200 mW. The optic axis of the LiNbO$_3$ crystals, the polarization of the pump and probe pulses, and the polarization of the generated THz wave are all parallel to the x axis. Unfortunately saw-cutting of the wafer resulted in a rough-textured surface so that the LiNbO$_3$ stripes are not transparent to the optical probe pulse. The reflection from and the transmission through the SRR arrays are therefore recorded in two separate measurements. For the reflection measurement a geometry as shown in Fig. 2 is used. For the transmission measurement the LiNbO$_3$ wafer stripes are reversed so that the SRR structures face the right crystal. Also, depending on whether the reflected or the transmitted wave is to be visualized either the part of the probe beam propagating through the left or through the right crystal is imaged onto the CCD camera. Compared to scanning techniques our approach has the advantage that two dimensional (2D) images showing the spatial distribution of the electric field can be recorded in real time. Also, since the sample is embedded in a homogeneous dielectric environment which directly serves as the electro-optic detection crystal we avoid using an external detector whose physical presence might influence the THz waveform.

Fig. 3 Schematic illustration
of the simulation geometry.
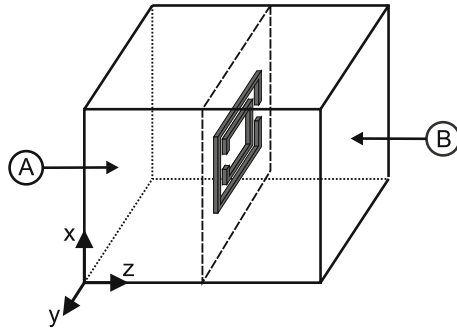
3 Simulations

We also perform 3D finite element method (FEM) [24] simulations in the
time domain. A schematic illustration of the simulation geometry is shown in
Fig. 3. SRR structures with dimensions identical with the structures used in the
experiment are positioned in the center of a block-shaped simulation domain.
Only the SRR thickness d is increased to 4 μm because a thickness of 400 nm
would result in a much larger number of mesh elements causing a significant
increase in computational demands. We note, however, that the spectral
response of SRRs is independent of their thickness as long as d is larger than
the skin depth [25]. In all simulations the refractive index of the surrounding
dielectric is set to $n = 5.11$. This value corresponds to the index of LiNbO$_3$
along the optic axis for frequencies below the lowest phonon mode [13]. The
simulation domain is discretized using a tetrahedral mesh and additional mesh
layers at all SRR interfaces are added in order to account for the different
length scales of the THz wavelength (~100 μm) and the interaction lengths in
metals (~100 nm). A broadband single cycle pulse is excited on boundary A.
Boundary B is set as a scattering boundary condition absorbing all incident
field components. The four other boundaries are set to periodic conditions
corresponding to an infinite SRR array and the size of the simulation domain
is chosen according to the periodicity of the fabricated structures.

4 Results

Figure 4 shows the reflection of a THz pulse from the original SRR array in a
temporal sequence.

The dashed white lines indicate the position of the SRR arrays and the red
arrows the propagation direction. The reflection process may also be viewed as
a movie in Online Resource 1. Figure 4a and b are a direct visualization of the
tilted pulse front excitation scheme. The leftmost part of the tilted pump pulse
creates two counter-propagating and initially weak THz waveforms (Fig. 4a).
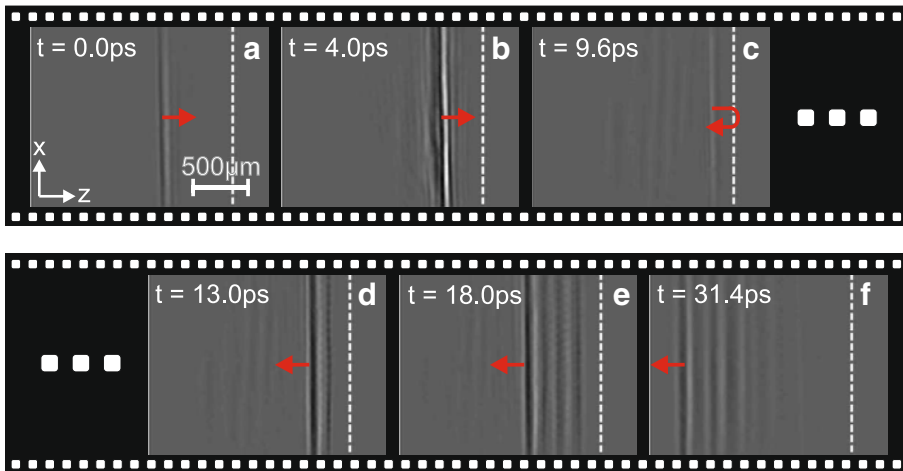The waveform propagating to the right increases its amplitude upon matched

Fig. 4 Temporal sequence showing the reflection of a THz pulse from the original SRR array (dashed line).

interaction with the tilted pump pulse until it reaches the rightmost part of the latter (Fig. 4b). When the THz pulse reaches the edge of the first crystal in Fig. 4c the signal disappears. The crystals used in the experiment are polished on all sides and the edges are slightly clipped under a 45° angle. This clipping results in a small blind region adjacent to the edge because the clipped corners are opaque for the probe pulse. One can, however, see that the THz pulse is party reflected at the SRR array and reappears in the image region in Fig. 4d. The waveform then continues to propagate to the left. A close inspection of Fig. 4e reveals that the reflected signal also features periodic modulations along directions intermediate to the z and x axes which are assigned to near-field interference of the scattered light as discussed later. After the reflected wave has propagated a certain distance away from the SRR sample it can be seen that the main oscillation cycle is followed by slowly decaying temporal ringing as shown in Fig. 4f. This ringing is a direct signature of the resonant response of the split-ring structures to the incident field.

One can see that the wavelengths of the inclined periodic modulations visible in Fig. 4e are much shorter than the estimated length of the main oscillation cycle. The behavior evidently exhibits a strong frequency dependance and is therefore best analyzed in the frequency domain. The data shown in Fig. 4 is composed of two spatial and one temporal dimension, i.e. $E(z, x, t)$. By applying a Fourier transformation for each spatial pixel we obtain the complex electric field distribution $\widehat{E}(z, x, \nu)$. The spatial distribution of the electric field at two exclusive frequencies is shown in Fig. 5a and b.

Whereas at 400 GHz the field distribution corresponds to a rather plane wave it exhibits a more complex pattern at 760 GHz featuring periodic modulations. We have additionally calculated the electric field distribution resulting from a linear array of 30 point sources as shown in Fig. 5c and d. The point

Fig. 5 Spatial distribution of the **a** 400 GHz and **b** 760 GHz frequency components of the THz pulse reflected from the original SRR array. Calculated field distribution assuming a linear array of point sources radiating at **c** 400 GHz and **d** 760 GHz.
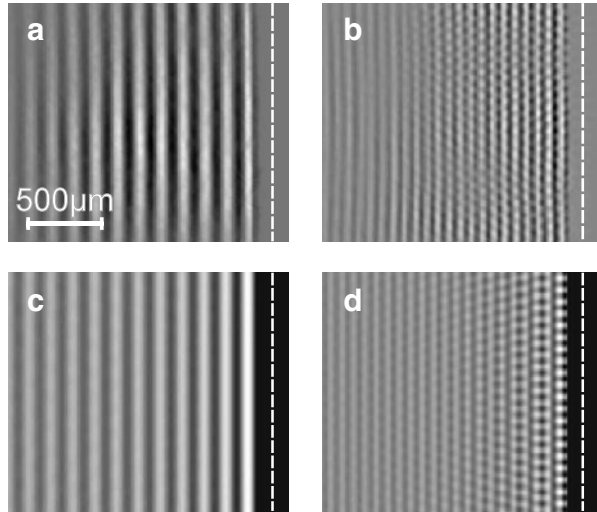
sources are positioned on the dashed line with a separation corresponding to the periodicity of the SRR array. The excellent agreement shows that the periodic modulation is due to interference of the radiation emitted by every individual SRR and that the spatial dependance is dominated by the lattice constant rather than the shape of the individual structures. For higher frequencies the periodic SRR array effectively acts as a grating [10]. The observed field distribution therefore corresponds to the near-field interference pattern of the different diffraction modes. Thus, the periodicity also determines the apparent frequency at which the modulation is switched on as well as the modulation direction. One can see that the further the THz wave propagates to the left, the more it evolves into a plane wave since the diffracted components leave the image region. Our setup therefore allows us to directly observe the near- to far-field evolution.

In Fig. 6 we plot a temporal sequence showing the interaction of a THz pulse with the SRR array as obtained from time dependant FEM calculations.
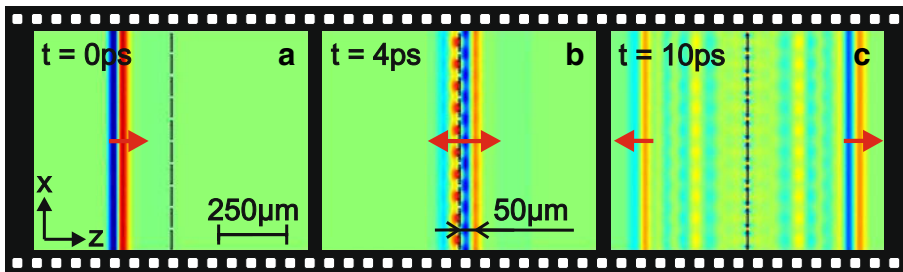

Fig. 6 Temporal sequence obtained from FEM simulations showing the interaction of the THz pulse with the SRR array.

The slice plot shows the electric field in a plane that cuts through the center of the split-rings. The SRRs' cross sections are marked by the black rectangles. Figure 6a shows the incident single cycle pulse. The spatial distribution of the pulse during the immediate transmission process can be seen in Fig. 6b, and Fig. 6c shows the partly transmitted and reflected waveforms. The simulation may also be viewed as a movie available in Online Resource 2. One can see that the simulation shows good agreement with the measured field distribution in Fig. 4. In particular the periodic modulations are visible in both the transmitted and reflected waveform. From Fig. 6b one can additionally see that during the immediate wave transmission each resonator is surrounded by strong electric fields. The different field components merge into a continuous wavefront after a propagation distance of only 50 μm. For the time step shown in Fig. 6b this can best be seen in the forward direction as indicated by the black arrow. Since this distance is smaller than the longitudinal extent of the blind region in our experimental setup we cannot directly resolve the strong electric fields surrounding the individual rings. We note, however, that there should be no physical limitation as to why visualization of the immediate near-fields should not be possible using $LiNbO_3$ crystals with a more precise rectangular cut.

The waveform reflected from the original SRR array is again shown in Fig. 7a together with the transmitted wave in Fig. 7b. In addition the corresponding plots obtained from measurements with the complementary structures are shown in Fig. 7c and d.

The images show the electric field distribution recorded approximately 25 ps after the interaction with the split-ring arrays. The complete spatiotemporal evolution of the waves in Fig. 7b–d are available as movies in Online Resource 3, 4, and 5. As expected the four waveforms exhibit significant differences in the temporal ringing. In order to analyze the spectral response of the split-
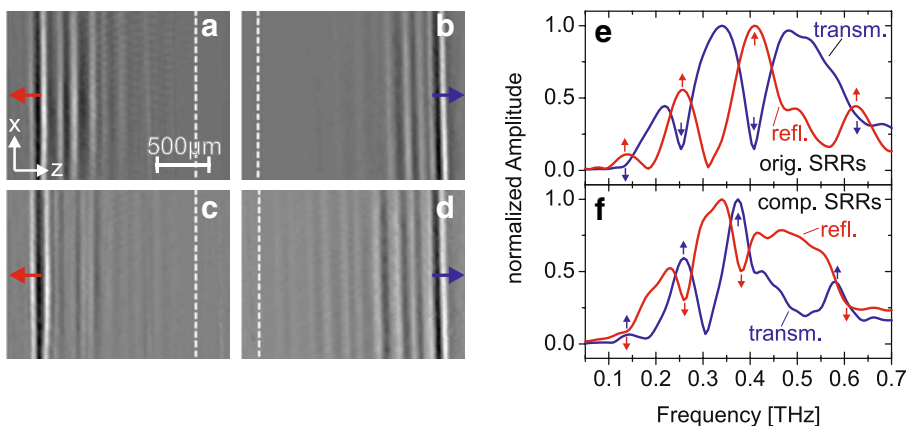

Fig. 7 Recorded waveform at some time step after the interaction with the SRR arrays. **a** Reflection from original SRRs, **b** transmission through original SRRs, **c** reflection from complementary SRRs, **d** transmission through complementary SRRs. Measured transmission and reflection spectra of **e** original and **f** complementary SRRs.

ring structures we plot in Fig. 7e and f the corresponding transmission and reflection spectra.

One can see from Fig. 7e that for the original SRR array the transmission spectrum (blue curve) features four dips at different frequency positions as marked by the arrows. The reflection spectrum (red curve) is approximately inverse to the transmission spectrum featuring four peaks. The dips and peaks correspond to the characteristic modes of the split-ring structures [11]. Since the SRRs are excited by the incident radiation and energy needs to be conserved the resonances manifest themselves through a decreased transmission, i.e. dips in the transmission spectrum. After excitation the SRRs oscillate and emit radiation at frequencies corresponding to their characteristic resonances. In the backward direction the SRR modes are therefore observed as peaks.

The transmission and reflection spectra of the complementary structures are shown in Fig. 7f. It has been shown previously [23] that according to Babinet's principle the transmission spectra of original and complementary SRRs for normal incidence are inverse if the polarization of the incident light field is rotated by 90° around the propagation axis. Rather than rotating the polarization we rotate the geometry of the corresponding structures as can be seen from Fig. 1. Whereas the original SRRs have the gap bearing side along the x direction the complementary structures were oriented to have the gap along y. In the transmission spectrum of the complementary array (blue curve in Fig. 7f) the SRR resonances are observed as peaks which is indeed complementary to the transmission through the original structures. Also, the reflection spectrum (red curve) is again seen to be approximately inverse to the transmission so that in this case the split-ring resonances are observed as dips.

5 Conclusion

The polaritonic approach was shown to be a powerful tool to visualize the electric field distribution of THz pulses transmitted through and reflected from metamaterials. It is especially well suited to bridge the gap between dedicated near-field and far-field techniques and offers the unique advantage to spatially resolve the interaction of the incident wave with the metamaterial structures. Moreover, no extra element is needed as in other near-field techniques, for example a metal tip or a metal aperture, and, thus, the measurement arrangement itself does not influence or even alter the near-field distribution in the vicinity of the split ring resonators.

The interaction of broadband THz pulses with planar arrays of original and complementary double SRRs was analyzed and the structures were found to exhibit inverse resonant behaviors in accordance with Babinet's principle. For both structures the spectra of the transmitted and reflected waveforms were also found to be complementary.

References

1. R. Shelby, D. Smith, and S. Schultz, Science **292**, 77 (2001).
2. J. Pendry, Phys. Rev. Lett. **85** (18), 3966 (2000).
3. J. Pendry, D. Schurig, and D. Smith, Science **312**(5781), 1780 (2006).
4. J. Pendry, A. Holden, D. Robbins, and W. Stewart, IEEE Trans. Microwave Theor. Tech. **47** (11), 2075 (1999).
5. C. Rockstuhl, F. Lederer, C. Etrich, T. Zentgraf, J. Kuhl, and H. Giessen, Opt. Express **14** (19), 8827 (2006).
6. M. van Exter and D. Grischkowsky, IEEE Trans. Microwave Theor. Tech. **38** (11), 1684 (1990).
7. A. Azad, J. Dai, and W. Zhang, Opt. Lett. **31** (5), 634 (2006).
8. H. Chen, J. Padilla, J. Zide, A. Gossard, A. Taylor, and D. Averitt, Nature **444**, 597 (2006).
9. R. Singh, E. Smirnova, A. Taylor, J. O'Hara, and W. Zhang, Opt. Express **16** (9), 6537 (2008).
10. A. Bitzer, J. Wallauer, H. Helm, H. Merbold, T. Feurer, and M. Walther, Opt. Express **17** (24), 22108 (2009).
11. A. Bitzer, H. Merbold, A. Thoman, T. Feurer, H. Helm, and M. Walther, Opt. Express **17** (5), 3826 (2009).
12. G. Acuna, S. Heucke, F. Kuchler, H. Chen, A. Taylor, and R. Kersting, Opt. Express **16** (23), 18745 (2008).
13. T. Feurer, N. Stoyanov, D. Ward, J. Vaughan, E. Satz, and K. Nelson, Annu. Rev. Mater. Res. **37**, 317 (2007).
14. A. Barker and R. Loudon, Rev. Mod. Phys. **44** (1), 18 (1972).
15. D. Auston and M. Nuss, IEEE J. Quantum Electron. **24**, 184 (1988).
16. A. Stepanov, J. Hebling, and J. Kuhl, Appl. Phys., B **81**, 23 (2005).
17. D. Auston, K. Cheung, J. Valdmanis, and D. Kleinman, Phys. Rev. Lett. **53** (16), 1555 (1984).
18. J. Hebling, G. Almasi, I. Kozma, and J. Kuhl, Opt. Express **10** (21), 1161 (2002).
19. A. Stepanov, J. Kuhl, I. Kozma, E. Riedle, G. Almasi, and J. Hebling, Opt. Express **13** (15), 5762 (2005).
20. R. Koehl, S. Adachi, and K. Nelson, J. Chem. Phys. **110**, 1317 (1999).
21. P. Peier, S. Pilz, F. Müller, K. Nelson, and T. Feurer, J. Opt. Soc. Am. B **25** (7), B70 (2008).
22. H. Merbold and T. Feurer, J. Appl. Phys. **107**, 033504 (2010).
23. H.T. Chen, J. O'Hara, A. Taylor, R. Averitt, C. High-strete, M. Lee *et al.*, Opt. Express **15** (3), 1084 (2007).
24. J. Jin, *The Finite Element Method in Electromagnetics*, 2nd ed. (Wiley-IEEE Press, New York, 2002).
25. M. Kafesaki, T. Koschny, R. Penciu, T. Gundogdu, E. Economou, and C. Soukoulis, J. Opt. A, Pure Appl. Opt. **7**, S12 (2005).